Application of Non-toxic Yield Stress Fluids Porosimetry Method and Pore-Network Modelling to Characterize the Pore Size Distribution of Packs of Spherical Beads

Antonio Rodríguez de Castro[1] · Mehrez Agnaou[2] · Azita Ahmadi-Sénichault[3] · Abdelaziz Omari[4]

Abstract

With X-ray computed tomography still being flawed as a result of limitations in terms of spatial resolution and cost, toxic mercury intrusion porosimetry (MIP) is nowadays the prevailing technique to determine PSDs of most porous media. Recently, yield stress fluids porosimetry method (YSM) has been identified as a promising clean alternative to MIP. This technique is based on the particular percolation patterns followed by yield stress fluids, which only flow through certain pores when injected at a given pressure gradient. In previous works, YSM was used to characterize natural and synthetic porous media, and the results were compared with MIP showing reasonable agreement. However, considerable uncertainty still remains regarding the characterized pore dimension with each method arising from the highly complex geometry of the interstices in real porous media. Therefore, a critical stage for the validation of YSM consists in achieving successful characterization of model porous media with well-known pore morphology and topology. With this objective in mind, a set of four packs of glass beads each with a given monodisperse bead size were characterized in the present work using different porosimetry methods: experimental YSM, numerically simulation of MIP and pore-network extraction from a 3D image. The results provided by these techniques were compared, allowing the identification of the pore dimensions being characterized in each case. The results of this research elucidate the causes of the discrepancies between the considered porosimetry methods and demonstrate the usefulness of the PSD provided by YSM when predicting flow in porous media.

Keywords Porosimetry · Yield stress fluids · Pore size distribution · Experimental method · Packed beds

✉ Antonio Rodríguez de Castro
  antonio.rodriguezdecastro@ensam.eu

1 Introduction

Pore size distribution (PSD) has a strong influence on both mechanical and transport properties of porous media, including uniaxial compressive strength (Hudyma et al. 2004; Li et al. 2018a, b), permeability (Zhang et al. 2016) and gas desorption time (Li et al. 2018a, b). Consequently, knowledge of PSD is essential in a wide range of industrial applications, e.g. soil remediation, CO_2 sequestration, oil and gas industry or geothermal energy generation. Nowadays, mercury intrusion porosimetry (MIP) is the standard technique of experimental determination of PSD (Giesche 2006; León y León 1998; Cieszko et al. 2019), due to the brief duration of the tests and the wide range of accessible pore sizes, i.e. ~ 1 nm to 1 mm (Zhang et al. 2016). However, the international scientific community is eagerly seeking effective clean alternatives to MIP (Rouquerol et al. 2012) due to the severe restrictions on the use of mercury (United Nations 2013). Some other limitations of MIP are the risk of damaging the original pore structure (Li et al. 2018a, b), and the indiscriminate filling of large and small pores downstream of the opening constriction (Diamond 2000). Also, X-ray micro-computed tomography is a powerful tool to characterize the 3D microstructure and the transport properties of a large number of porous media (Lindquist and Venkatarangan 2000; Burlion et al. 2006; Prodanovic et al. 2006; Wildenschild and Sheppard 2013; Bultreys et al. 2016; Houston et al. 2017). Nevertheless, the required instruments are costly and the technique is limited by the spatial resolution (of the order of 1 μm), the long acquisition and reconstruction times, the use of poorly representative thin samples and the user-dependent filtering and segmentation stages. Other usual porosimetry methods, such as nitrogen or water-desorption porosimetry (Rouquerol et al. 2012; Bultreys et al. 2016), require extremely elaborated preparation of the samples and the test times are long. The combination of several techniques is the only option to fully characterize PSDs covering many orders of magnitude in size (Bultreys et al. 2016; Li et al. 2018a, b; Wang et al. 2018; Chen et al. 2018; Alfi et al. 2019).

Ambari et al. (1990) presented the theoretical aspects of a novel porosimetry method based on the derivation of the PSD from the flow rate Q versus pressure gradient ∇P measurements obtained during the injection of a yield stress fluid through a porous sample. This method was based on modelling the porous medium as a bundle of straight cylindrical capillaries of circular cross section with different radii. Only the special case of a Bingham fluid without shear-thinning behaviour was addressed by the latter authors, but the theoretical method was subsequently extended to the more general case of Casson and Herschel–Bulkley fluids (Oukhlef 2011; Oukhlef et al. 2014). Moreover, Oukhlef et al. (2014) achieved analytical inversion of numerically generated Q versus ∇P data sets corresponding to the injection of a yield stress fluid through a bundle of capillaries. In the preceding work, the PSD was successfully determined by computing the partial derivatives of a continuous polynomial regression of the numerical $Q(\nabla P)$ data. However, the analytical inversion was deeply sensitive to experimental uncertainty, and it was limited to rational values of the flow index of the yield stress fluid and provided noisy results in the small pore size region. Therefore, an alternative numerical inversion using polynomial filtering was proposed by (Malvault 2013) to obtain the PSDs of model porous media from laboratory experiments. A major shortcoming of this alternative inversion was the strong dependence of the obtained PSD on the order of the polynomial filtering.

Building on the preceding developments and theoretical considerations, the yield stress porosimetry method (YSM) was presented (Rodríguez de Castro et al. 2014), which used an inversion procedure in which no filtering or interpolation of the raw experimental data

is needed. YSM consists in isolating the contribution of the extra flow rate occurring only in the pores of increasingly smaller size in which the yield stress fluid starts to flow when the pressure gradient is steeply increased. Then, from this isolated contribution, the number of pores of the incorporated pore size class can be calculated. After considering the main advantages and drawbacks of using different candidate yield stress fluids, including oil-in-water emulsions and Carbopol suspensions, xanthan gum aqueous solutions were selected by Rodríguez de Castro (2014). This choice was primarily motivated by the low degree of visco-elasticity (Jones and Walters 1989; Sorbie 1991) and the negligible thixotropy exhibited by the solutions of xanthan gum macromolecules. Moreover, polymer retention, mechanical degradation and adsorption of the macromolecules in different types of commonly encountered natural and synthetic porous media were experimentally assessed by Rodríguez de Castro et al. (2016), concluding that none of these effects was significant apart from polymer retention at very low flow rates in less permeable porous media. Furthermore, Rodríguez de Castro et al. (2018) investigated the effects of polymer concentration of xanthan solutions on the accuracy of the PSDs provided by YSM, and the sensitivity of the method to errors in the experimental determination of the shear-rheology parameters. In the latter work, nominal values of polymer concentration were proposed for porous media with high-to-moderate permeability.

Despite the progress made in the preceding works, none of them focused on identifying the pore dimension provided by YSM through comparison with a 3D image of the microstructure, so further interpretation of the results remains a serious challenge. To solve this issue, the aim of the present work is to validate YSM in the case of well-characterized packs of spherical beads. Moreover, the nature of the pore dimensions provided by this method will be elucidated. To achieve that goal, a set of YSM tests are performed by injecting a concentrated polymer solution through different packs of monodisperse spherical glass beads. The obtained $(Q, \nabla P)$ data sets are then used as inputs to the YSM algorithm, allowing the computation of the PSDs. To go further, the bodies-and-throats network of a digital 3D image of a pack of identical spheres is also extracted and used to perform a numerical simulation of a MIP test. By doing so, the PSDs obtained with YSM can be compared to the equivalent PSDs obtained by MIP. The PSDs obtained by both methods are then compared to the body and throat size distributions of the extracted pore network, facilitating the identification of the characterized pore dimension in each case. It should be noted that performing MIP laboratory tests to characterize unconsolidated porous media is known to be extremely challenging (Minagawa et al. 2008) due to the weak cohesion between particles and deformation of the pore network, so simulated MIP is a particularly useful alternative in the case of the present application.

2 Extracting Pore Size Distribution by Using Yield Stress Fluid Porosimetry Method

The details of the procedure followed to obtain the PSD from the raw $(Q_i, \nabla P_i)$ data collected during injection of a yield stress fluid in a porous sample were provided by Rodríguez de Castro et al. (2014, 2016, 2018). For this reason, only the essential features of the method are presented in this section.

Herschel–Bulkley's law (Eq. 1) is the rheological model used in YSM to describe the dependence of shear stress on shear rate for yield stress fluids under steady-state simple shear conditions.

$$\begin{cases} \tau = \tau_0 + k\dot{\gamma}^n & \text{for } \tau \geq \tau_0 \\ \dot{\gamma} = 0 & \text{for } \tau \leq \tau_0 \end{cases} \qquad (1)$$

with τ_0, k and n being the yield stress, the consistency and the flow index of the fluid, respectively. The preceding bulk rheological parameters are empirically determined with a controlled-stress rheometer.

Figure 1 provides a flow chart describing the steps YSM algorithm for the calculation of the PSD. A standard YSM test consists in collecting a set of $(Q_i, \nabla P_i)$ data during the injection of a Herschel–Bulkley fluid through a porous sample. From these $N+1$ measurements $(i=1\ldots N+1)$, a set of N representative pore radii are defined as:

$$r_j = \alpha \frac{2\tau_0}{\nabla P_j} \quad (j = 1 \ldots N)$$

It must be borne in mind that the flow of a yield stress fluid at a given ∇P_j only occurs in the pores with a radius strictly larger than $\frac{2\tau_0}{\nabla P_j}$. Consequently, the value of the numerical factor α must be greater than unity. A full description of the procedure followed to calculate the value of α was provided in previous works (Rodríguez de Castro 2014; Rodríguez de Castro et al. 2014), and the main steps are represented in Fig. 1. In this procedure, the number of pores n_j of the class r_j is calculated as being the maximum positive value of n_j for which the following condition is respected:

$$Q_s \geq \sum_{g=1}^{j} n_g q(\nabla P_s, r_g) \quad \text{for } s \geq j+1$$
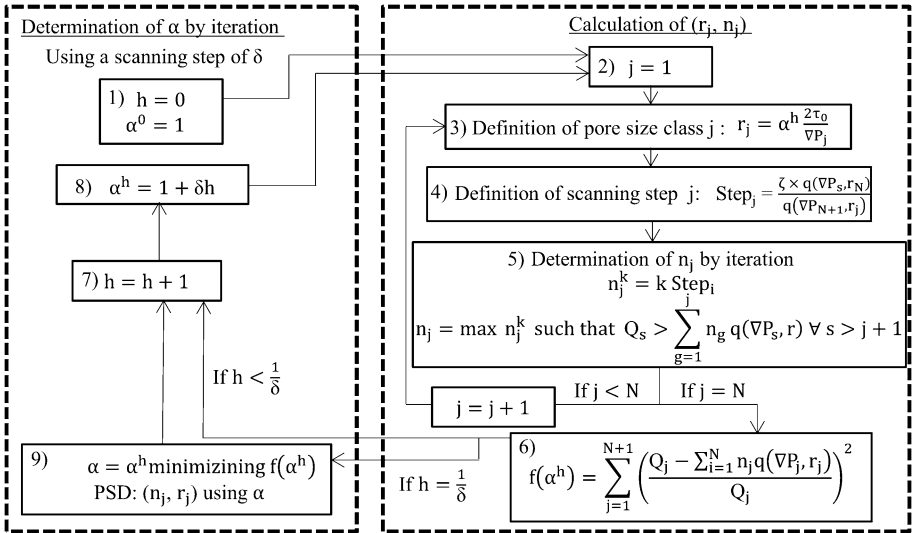
Fig. 1 Algorithm for the calculation of the PSD from a set of $(Q_j, \nabla P_j)$ data by using YSM [details were provided by Rodríguez de Castro et al. (2016)]. The scanning steps were $\zeta = 0.05$ and $\delta = 0.1$ in the present experiments

where $q\left(\nabla P_s, r_g\right)$ is the volumetric flow rate of a Herschel–Bulkley fluid through a cylindrical capillary of radius r_g as a function of ∇P_s, as given by Skelland (1967) and Chhabra and Richardson (2008). The number of biggest pores n_1 is first calculated, and then the number of smaller and smaller pores is determined until n_N (the number of the smallest pores) is computed. Moreover, the relative frequency of each pore class r_j can be calculated as:

$$p\left(r_j\right) = \frac{n_j}{\sum_{i=1}^{N} n_i}$$

It should be noted that in the scanning procedure to calculate each n_j, and as large pores contribute significantly to the total flow rate, the scanning should be more refined when the considered pore radius is large. The step used in the scanning procedure is: $\text{Step}_j = q\left(\nabla P_s, r_N\right)/q\left(\nabla P_{N+1}, r_j\right)$, where ζ is an index that determines the refinement of scanning ($\zeta = 0.05$ was used in the present experiments). Also, to determine the suitable value of α, named α^*, successive increasing values are used to calculate the PSD, from $\alpha = 1$ to $\alpha = 2$ with a scanning step of δ ($\delta = 0.1$ was used in the present experiments). α^* is the value of α that minimizes the least squares relative difference between calculated (through Eq. 2) and experimental (Q_i, ∇P_i) data.

From the obtained PSD, the macroscopic flow law expressing the relationship between the total flow rate through the medium Q and the pressure gradient ∇P can be computed as:

$$Q(\nabla P) = \sum_{i=1}^{N} n_i q\left(\nabla P, r_i\right) \tag{2}$$

3 Experimental Set-up and Procedure for the Yield Stress Fluid Porosimetry Method Tests

In the present experiments, a 7000-ppm xanthan gum aqueous solution was injected through the investigated packs of beads during the YSM tests. The choice of this concentration of xanthan gum solution to perform the (Q_i, ∇P_i) measurements was motivated by the results presented by Rodríguez de Castro et al. (2018), in which this concentration was identified as a reliable one for the injection fluid used in YSM when dealing with porous media with high-to-moderate permeability (typically > 50 mD). These concentrated aqueous solutions featured extremely high viscosity values at low shear rates, closely approaching the behaviour of ideal yield stress fluids without showing significant thixotropy or visco-elasticity. Moreover, and this is a strict condition, the fluid is not toxic.

The microbial biopolymer xanthan is an exo-polysaccharide with high molecular weight (Garcia-Ochoa et al. 2000; Palaniraj and Jayaraman 2011; Kumar et al. 2018). The stiff macromolecules of this polymer confer very high viscosity values to the concentrated aqueous solutions under low shear rate conditions. Moreover, xanthan solutions are strongly shear-thinning, exhibiting a decrease in viscosity with increasing shear rate as a result of the orientation of the macromolecules in the direction of flow. For these reasons, the steady-state shear rheology of xanthan gum solutions is adequately described by the Herschel–Bulkley empirical law (Eq. 1), as supported by previous research (García-Ochoa and Casas 1994; Song et al. 2006; Rodríguez de Castro et al. 2016; Dakhil et al. 2019, Rodríguez de Castro 2019). However, although the shear viscosity of xanthan gum polymer solutions at low shear rates is very high, its value is finite. Consequently, xanthan solutions are more accurately termed as pseudo-yield stress fluids exhibiting an apparent yield stress

Fig. 2 a Rheogram of the 7000-ppm xanthan gum aqueous solution and **b** viscosity versus shear rate relationship. The black symbols represent experimental measurements, and black solid lines represent Herschel–Bulkley model fit (Eq. 1)
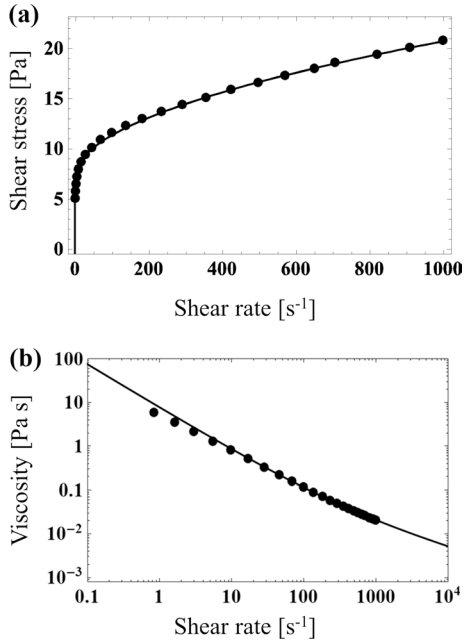
Table 1 Porosity, permeability, injection velocities and number of experimental data for the experiments with the four different beads sizes

d_s (mm)	ε (–)	K (m²)	Range of u (m/s)	$N+1$
1	$0.36 \pm 0.1\%$	$5.9 \times 10^{-10} \pm 2\%$	1.7×10^{-5}–3.5×10^{-3}	27
3	$0.34 \pm 0.1\%$	$5.1 \times 10^{-9} \pm 6\%$	8.5×10^{-5}–2.1×10^{-2}	26
4	$0.35 \pm 0.1\%$	$9.5 \times 10^{-9} \pm 7\%$	1.7×10^{-5}–2.1×10^{-2}	34
5	$0.34 \pm 0.1\%$	$1.3 \times 10^{-8} \pm 6\%$	1.7×10^{-5}–2.8×10^{-2}	33

(Withcomb and Macosko 1978; Carnali 1991; Song et al. 2006; Khodja 2008; Benmouf-fok-Benbelkacem et al. 2010). In this regard, it must be emphasized that it is of practical interest in many cases to consider that concentrated xanthan gum solutions have a yield stress.

In this work, 60 L of solution was produced with the selected polymer concentration $C_p = 7000$ ppm, and their rheological behaviour was characterized in terms of $(\tau, \dot{\gamma})$ steady-state measurements (Fig. 2) by adopting the procedure reported by Rodríguez de Castro et al. (2014) and Rodríguez de Castro (2019). Then, the rheogram was fitted by using Herschel–Bulkley model (Eq. 1), obtaining $\tau_0 = 7.4$ Pa, $k = 0.37$ Pa s^n and $n = 0.52$. The obtained fitting function is also represented in Fig. 2.

The weight of each packed bed was measured before and after saturation with water in order to determine the porosity, ε, from the difference in mass. Moreover, the permeability, K, was determined through water-injection experiments. The porosities and permeabilities of the characterized porous media are listed in Table 1, together with the associated uncertainties (95% confidence interval). The length of all the packed beds was 20 cm, and their inner diameter was 5 cm. It should be noted that ε and K are not needed as inputs to YSM

method, but are presented here for further comparison and analysis. As expected, porosity values are nearly identical for the four cases studied here and the permeability values follow the same trend as those given by Ergun's law for packed beds of spheres, i.e.:

$$K = \varepsilon^3 d_s^2 / \left(180(1-\varepsilon)^2\right)$$

with d_s being the diameter of the spherical beads.

A wide range of flow rates, within the limits of creeping flow, was investigated in the present experiments. Depending on the targeted flow rate, two different set-ups were used. An open circuit equipped with a dual piston pump was used for flow rates between 0.12 and 6 L/h while the circuit was closed and equipped with a volumetric pump for the higher flow rates ranging from 9 to 250 L/h. Further details of the equipment were provided by Rodríguez de Castro and Radilla (2017b). The yield stress fluid was injected through the investigated media, performing four repetitions of each flow experiment. Table 1 lists the number $N+1$ of $(Q_i, \nabla P_i)$ experimental data points obtained for each porous column. The range of Darcy velocities, $u_i = Q_i/A$, covered by the measurements is also provided in the same table, with A being the cross-sectional area of the columns. The $4 \times (N+1)$ measurements for each medium constituted an experimental data set. Further technical specifications can be consulted in a preceding work (Rodríguez de Castro and Radilla 2017a), e.g. the experimental uncertainties and the working ranges of the used equipment. Moreover, in order to evaluate the effects of polymer mechanical degradation and retention on the walls of the beads, the rheograms of several effluent samples were compared to that of the inflowing fluid. These rheograms were very similar, as expected, given the small size of the polymer molecules as compared to the size of the pores and their flat monolayer adsorption on pore walls (Mongruel and Cloitre 2003; Chauveteau 1982; Sorbie 1991; Dario et al. 2011), so both mechanical degradation and retention were neglected. The maximum Reynolds number Re attained during the laboratory experiments in the four packed beds was $Re = 2.62 \times 10^{-2}$, with Re being defined as:

$$Re = \frac{\rho u \sqrt{K}}{\mu^*}$$

where ρ is the density of the xanthan aqueous solution (taken as 1000 kg/m^3) and μ^* is the shear viscosity of the fluid in the porous media at u, which was calculated as described by Rodríguez de Castro (2019). Also, the maximum inertial pressure losses were evaluated as explained in the preceding reference, and were found to be lower than 4% in all cases. Therefore, creeping flow conditions were satisfied.

4 Extracting Pore Size Distribution from Digital Images

4.1 Pore-Network Modelling Approach

It was shown recently in a study (Yang et al. 2016), where multiple numerical approaches were used to simulate porous media fluid flow and solute transport at the pore scale, that the pore-network modelling approach provides reasonably accurate results with much less computational costs compared to direct numerical simulations. In this study (Yang et al. 2016), the used numerical approaches consist of the finite volume method, the lattice Boltzmann method, the smoothed particle hydrodynamics and the pore-network modelling. A pore network is a simplified representation of the porous medium. It consists of a set of pores interconnected

by throats. Idealized shapes are assigned to pores and throats for simplicity. In general, pores and throats are represented by spheres and cylinders, respectively. In the mixed-cell method, adopted in this study, perfect mixing within the pore space is assumed and the void volume of the porous medium is assigned to the pores. On the other hand, the throats size is taken into account in the calculation of the conductance between the neighbour pores. This approach offers simplicity and allows for pore-scale simulations at significantly lower computational costs compared to the continuum methods such as the finite volume method. Moreover, the extraction of a representative elementary volume (REV), which is not always easy as the REV's size was shown to vary with the Reynolds number even on ordered structures (Agnaou et al. 2016, 2017), is not required with this method. A freely available digital 3D image of a pack of identical spheres obtained by Finney (1970, 2016) was used in the current analysis, as will be presented in Sect. 5.3. The pack of spheres used by the latter author was generated by shaking together monodisperse 1/4-in-diameter steel ball-bearings, and the 3D image was optically obtained using a special marking technique. The same image was also used in other works, e.g. by Bijeljic et al. (2013). The porosity ε of the densest part of the packing, i.e. the central part, was approximately 36%. This porosity value is very close to those of the packs of spherical beads used in the YSM experiments presented in the preceding section (see Table 1), which facilitates comparison of the results.

For the pack of spheres considered in this work, the 3D digital image was used to extract the modelled network of pores. Pore-network extraction operations were performed using the subnetwork of the oversegmented watershed (SNOW) algorithm (Gostick 2017a, b). This algorithm is available on the open-source toolkit for quantitative analysis of porous media images, PoreSpy (Gostick et al. 2019). It can be applied to different types of porous media, which makes it a good choice for this work. In addition, it is implemented in Python which makes it easily extensible and relies on the Scipy stack which allows for a relatively short extraction time. The SNOW algorithm proceeds through different steps (Gostick 2017a, b) where it first extracts the distance map of the void spaces, filters it and eliminates peaks on saddles and plateaus. It then merges peaks that are close to each other. Finally, it assigns void voxels to pores. The same image was scaled to each of the bead sizes considered in this work using ImageJ software. Then, the resulting modelled pore network corresponding to each one of the packs of spheres was then used for mercury intrusion porosimetry simulations as described as follows.

4.2 Numerical Mercury Intrusion Porosimetry

The modelled pore structure obtained from the extraction operations using the SNOW algorithm was used to perform mercury intrusion porosimetry simulations. The open-source pore-network modelling package OpenPNM (Gostick et al. 2016) was used. First, the networks files, containing all the necessary network and geometrical information, are imported using an OpenPNM script. In a second step, the OpenPNM MIP algorithm in its standard version was used to perform simulations and obtain PSDs. This algorithm is based on the Washburn equation (Washburn 1921) for a given pore radius r_i:

$$r_i = -\frac{2\sigma \cos \theta}{P_{ci}} \tag{3}$$

by assuming a contact angle $\theta = 140°$ and a surface tension of the mercury–air pair $\sigma = 0.48$ N m^{-1}, which are routinely used values commonly accepted by most researchers (Giesche 2006). In the preceding equation, P_{ci} is the external pressure applied to mercury.

It should be noted that the PSD provided by MIP is volume-weighted, as it defines the volume fraction of pores that are accessible through pore openings of a given size (Cieszko et al. 2019). For each pack of spheres, simulations are performed over a range of pressure values. The resulting invading phase saturation (mercury) is then used to estimate the pore and throat sizes of the porous medium under study. This is achieved by calculating the volume-weighted probability of the pore size class r_i from the increment in mercury saturation when the applied pressure is increased from P_{ci-1} to P_{ci}.

5 Results

5.1 Raw Data Measured During the Yield Stress Fluid Method Tests

The results of the YSM experiments are presented in Fig. 3, with $u = Q/A$ being Darcy velocity. The errors bars represented in the mentioned figure correspond to a 95% confidence interval of the combined uncertainty related to the repeatability of the measurements and the accuracy of the pressure drop sensors. From these measurements, it can be deduced that the relationship between u and ∇P is nonlinear. Moreover, higher pressure drops were obtained in the columns filled with small beads, as expected given the lower permeability of these media. It is also observed that the u versus ∇P plots of the left side of Fig. 3 are similar in form to the τ versus $\dot{\gamma}$ rheograms presented in Fig. 2, due to the existing relationships between the pairs of variables τ–∇P and $\dot{\gamma}$–u. Also, a decrease in one order of magnitude in ∇P results in smaller values of u by
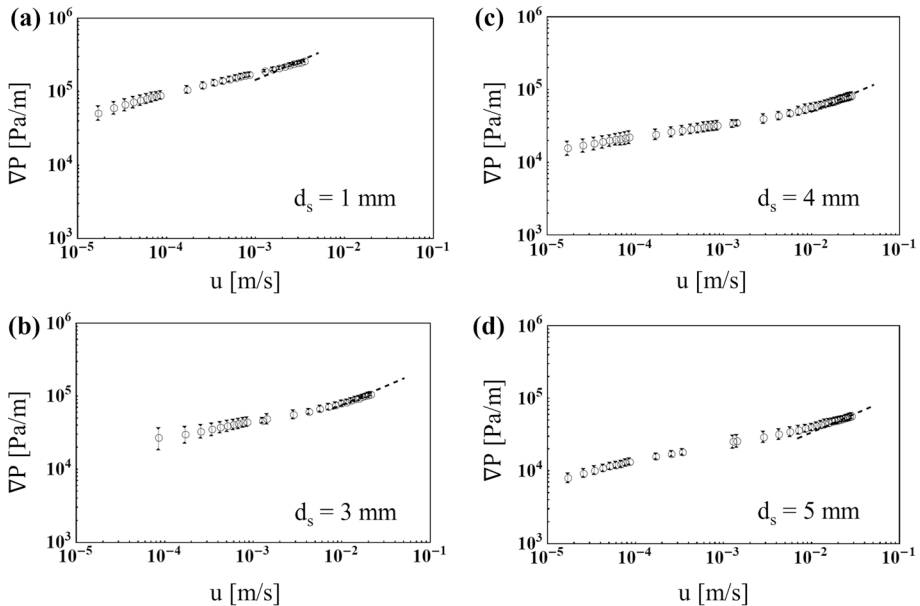
Fig. 3 Raw u–∇P measurements plots obtained from YSM experiments. These data points are used as input to the algorithm allowing the determination of PSD. **a–d** correspond to the different bead sizes. Dashed lines represent a power law of ∇P with an exponent of $1/n$ fitted to the data points corresponding to the four highest flow rates for each case (as discussed in Sect. 5.5)

Fig. 4 PSDs obtained with YSM for the four columns of packed beads
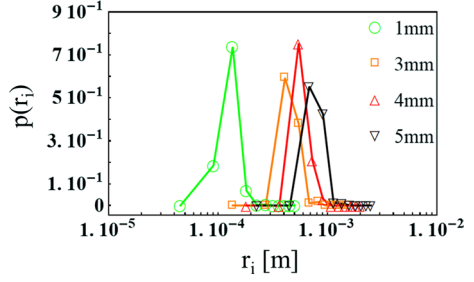
Table 2 Average (r_{av}) and peak (r_{peak}) radii of the PSD as determined from YSM tests

| d_s (mm)	r_{av} (μm)	r_{peak} (μm)
1	131	136
3	496	409
4	645	545
5	762	682

3-to-4 orders of magnitude. Therefore, it is confirmed that the injected fluid exhibits its strong shear-thinning behaviour in the porous media, in particular at the lowest injection velocities, which is the most distinctive pattern of a yield stress fluid. It is reminded that a threshold pressure gradient below which no flow is produced is a distinctive characteristic of ideal yield stress fluid. Similarly, in the realistic case of fluids with apparent yield stress as the injected concentrated xanthan gum solution, a pressure gradient exists below which the flow rate is negligible, as already reported in previous works (Rodríguez de Castro et al. 2014, 2016, 2018; Rodríguez de Castro and Radilla 2017b).

5.2 Pore Size Distribution Obtained with the Yield Stress Fluid Method

The procedure presented in Sect. 2 was applied to obtain the PSDs of the four packs of beads from the raw (u_i, ∇P_i) measurements, leading to the results presented in Fig. 4. The most significant aspect is that the PSDs are arranged in a consistent manner, with increasing pore sizes as the bead diameter is increased. To facilitate analysis, the average radii r_{av} and the frequency peaks r_{peak} of the PSDs presented in Fig. 4 are summarized in Table 2. It should also be remarked that the shape of the calculated PSDs is very similar, independent of the size of the spherical beads. Another conspicuous feature of the PSDs is their narrowness, with frequencies being significant only for the pore radius classes contiguous to the peak value. This can be interpreted as a signature that only a small region of the converging–diverging geometry of the interstices between beads is controlling the total pressure drop throughout the media, which is expected to exclude the largest zones of the pores (pore bodies). Indeed, in spite of the tortuous flow pathways, the pore space presents quite regular shape and topology, with a certain degree of periodicity due to the presence of identical spheres.

5.3 Pore Size Distribution Obtained with Pore-Network Modelling

Application of the method presented in Sect. 4.1 to the digital image of a real pack of beads displayed in Fig. 5a led to extraction of the modelled pore network displayed in Fig. 5b. An enlarged part of the network is also displayed in Fig. 5d in order to facilitate legibility. This pore network is composed of spherical pore bodies, accounting for all pore volumes, linked by cylindrical pore throats representing pore constrictions, which control pressure drops throughout the medium. The body size distribution (BSD) and throat size distribution (TSD) were also determined from the extracted pore network and are represented in Fig. 5c, after normalization by the sphere radius r_s. It is remarked that both the BSD and TSD are relatively narrow, with a single peak of high probability close to $r_i/r_s = 0.425$ and $r_i/r_s = 0.225$, respectively. The ratio between the two probability peaks can be interpreted as being an estimator of the pore-to-throat size ratio, obtaining a value of 1.89 in the present case, which is close to the pore-to-throat size ratio previously reported for packs of monodisperse beads (Grattoni 1994) and permeable sandstones (Rodríguez de Castro et al. 2016). This allows the quantification of the intensity of cross-sectional variation during
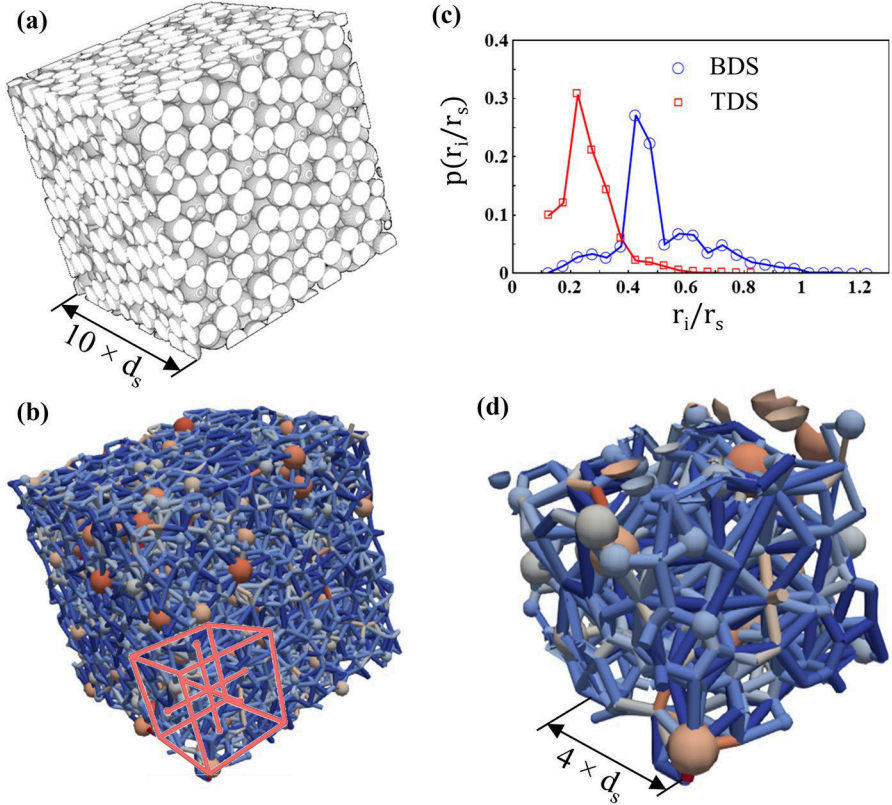
Fig. 5 Illustration of the pore-network modelling approach. **a** original digital image of a pack of spherical beads obtained by Finney (1970, 2016) through optical measurements. **b** Extracted 3D pore network. Darker colours represent bigger dimensions. **c** Body and throat size distributions (BDS and TDS) of the pore network, with normalized radius in the horizontal axis. **d** Enlarged image of the part of the network contained within the cubic volume of edge length $4 \times d_s$ represented in **c**

flow of the injected fluid throughout the media, and highlights the importance of selecting a fluid with non-significant extensional viscosity within the explored range of flow rates. Moreover, the same analysis can be performed by using digital images coming from 3D microtomography experiments, which represents a promising landscape for the validation and calibration of alternative porosimetry methods as YSM with a wide range of porous media. It should be borne in mind that, while wider size distributions are expected in porous rocks and other natural porous media (Wang et al. 2018; Wu et al. 2018; Alfi et al. 2019), the use of model porous media with well-defined pore and throat sizes is a mandatory stage for the evaluation of the reliability and accuracy of YSM results. The effects on PSD of the standard deviation of the sphere sizes in different types of packed lattices were investigated by Nolan and Kavanagh (1994) through numerical computations and can be used in future validation of YSM for polydisperse packs of beads.

5.4 Pore Size Distribution Obtained with Numerical Mercury Intrusion Porosimetry

The numerical MIP method presented in Sect. 4.2 was applied to the modelled pore network extracted from the digital image of the pack of equal spheres, providing the capillary pressure curve presented in Fig. 6a. Pa $\cdot r_s$ is represented in the horizontal axis of Fig. 6a in order to facilitate re-scaling for the different values of r_s and computation of the normalized PSD shown in Fig. 6b, which is independent of the value of r_s. It can be observed that the obtained capillary curve is monotonically increasing with an abrupt transition from initial to full saturation at pressure values close to 3 Pa $\cdot r_s$. This means that the whole pore space is saturated once the threshold value is exceeded. The pressure threshold can be interpreted as being the capillary pressure in the smallest openings to pore bodies. From this capillary pressure curve, the corresponding MIP–PSD can be calculated using Eq. (3), as displayed in Fig. 6b. The obtained distribution only presents a high-probability peak and is narrow, as expected from the sharp increase in saturation. It is noted that, although the PSD provided by MIP is volume-weighted, the results shown in Fig. 6b are already converted into frequency-weighted in order to facilitate comparison with the other methods.
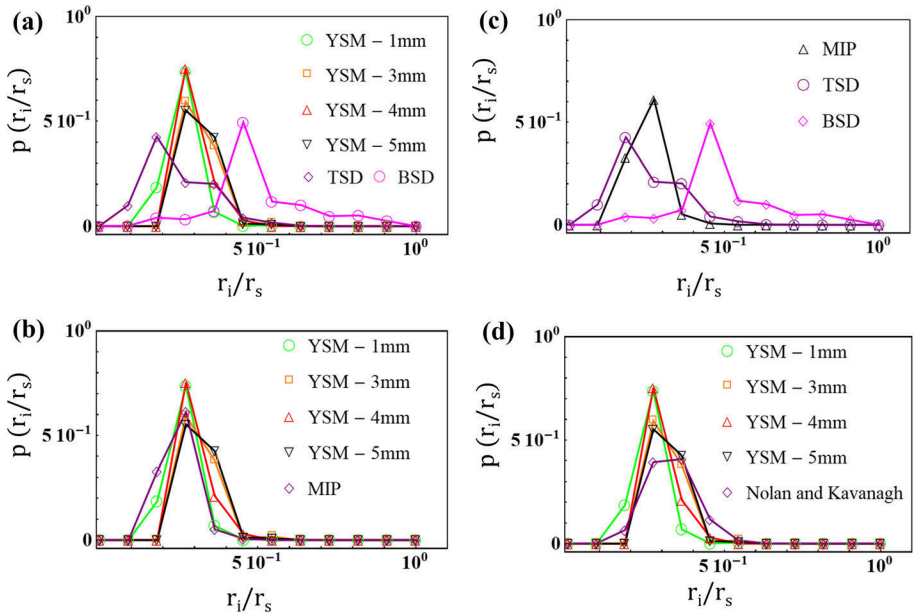
5.5 Comparison Between Methods

The results provided by YSM were compared to those obtained by MIP numerical simulations, structure analysis of the network model and the numerical simulations performed by
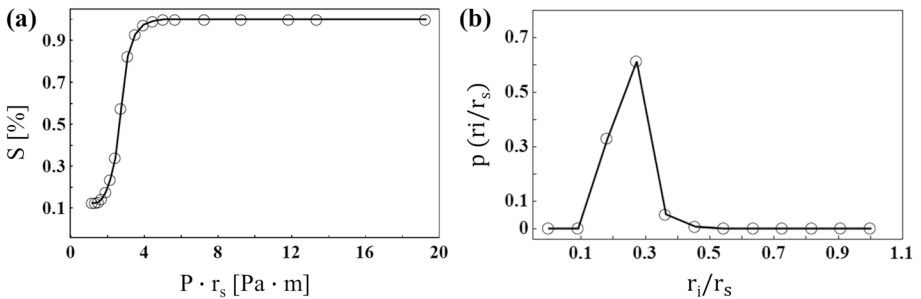
Fig. 6 Results of the numerical simulation of mercury intrusion porosimetry. **a** Capillary pressure curve. **b** Normalized pore size distribution

Nolan and Kavanagh (1994), which computed the PSD of a packing of spherical particles from the sizes of the largest spheres that can fit inside the interstices. To do such comparison, the PSDs were first normalized by the radius of the spherical beads r_s. By doing so, Fig. 7 shows that the PSDs obtained by YSM for all the investigated packs of beads collapse, independent of the radius of the spherical beads. It is observed in Fig. 7a that the range of pore sizes PSD obtained with YSM is comprised between the range of bodies and throats determined through the analysis of the pore-network model. It is observed in the same figure that YSM yields distributions that are closer to the sizes of the throats, which is expected given the nature of the performed measurements. Indeed, the pressure drop measurements conducted during a YSM test are more sensitive to the dimensions of the throats, in which stronger pressure drops are generated. In particular, when all pores are conducting, the overall flow rate at high pressure gradients ($\nabla P \gg \frac{2\tau_0}{r_0}$ where r_0 is the radius of the smallest pore in the porous medium) is a power law of ∇P with an exponent of $1/n$, as represented in Fig. 3.

The results obtained with YSM are in very good agreement with those provided by numerical MIP. The size distributions obtained by both techniques are represented in Fig. 7b, showing that the probability peaks coincide ($r_i/r_s = 0.27$) and the range of pore sizes is almost identical. Moreover, the averages values $E[r_i/r_s]$ of the obtained distributions are also very close, with $E[r_i/r_s] = 0.30$ for YSM and $E[r_i/r_s] = 0.27$ for MIP. It must be highlighted that the PSD obtained by MIP falls within the region of the pore throats (Fig. 7c), which is consistent with the measuring principle of this method, sensitive to the largest openings to pore bodies. Additionally, the YSM-PSDs were also compared to the


Fig. 7 Comparison between the three investigated methods. **a** YSM versus pore-network model, with TSD and BSD being the throat and body size distributions, respectively. **b** YSM versus simulated MIP. **c** MIP versus pore-network model. **d** YSM compared to the PSDs computed by Nolan and Kavanagh (1994). In all cases, r_i is normalized by sphere radius r_s

numerically computed PSDs performed by Nolan and Kavanagh (1994) using random close-packed lattices of equal spheres, and the results showed also mutual agreement as depicted in Fig. 7d. Also, the PSDs obtained in the paper using YSM and MIP are compared in Fig. 8 with the results of direct determination of PSD based on pure geometrical analysis of the digital image applying the widely used method of maximum inscribed ball into the pore space (Hildebrand and Ruegsegger 1997). This method can be considered as a "gold standard" for the determination and PSD, and was previously compared in detail to the SNOW algorithm used in the pore-Network analysis presented in Sect. 4.1 (Gostick 2017a, b). As can be deduced from Fig. 8, the agreement between the TSD provided by the maximum inscribed ball algorithm, MIP and YSM is very good, and the predicted class of maximum probability is the same for the three methods.

6 Discussion

In contrast with the findings of this paper, previous experiments performed on samples of real sandstones and sintered silicates showed that YSM provided smaller pore sizes than MIP (Rodríguez de Castro et al. 2016, 2018), and the reasons were discussed. Careful analysis leads to the conclusion that whereas the openings towards pore bodies are all of similar size in the packs of identical beads, which is also the size of the pore constrictions controlling pressure drop, this is not necessarily the general case for other media of higher complexity in which pore sizes span a wide range. In this respect, the higher tortuosity values and the irregular shapes of consolidated grains may also play a crucial role in explaining the discrepancies between YSM and MIP for natural porous media. It is reminded that the measured quantities are different in each method, e.g. pressure drop in YSM and capillary pressure in MIP. Consequently, YSM is especially sensitive to the diameter of pore throats, while the characterized pore dimension is the largest entrance towards a pore body in the case of MIP. The values of both dimensions are expected to be close in the case of uniform packs of spherical beads, which is consistent with the present results. This is also consistent with the results of Chauveteau et al. (1996), who found that the characterized dimension with MIP was approximately 1.2 times larger than the pore throat dimension in the case of unconsolidated granular packs of beads, while it was approximately 1.9 times larger for consolidated sandstones. In the same works, the authors highlighted that MIP remained a static non-directional
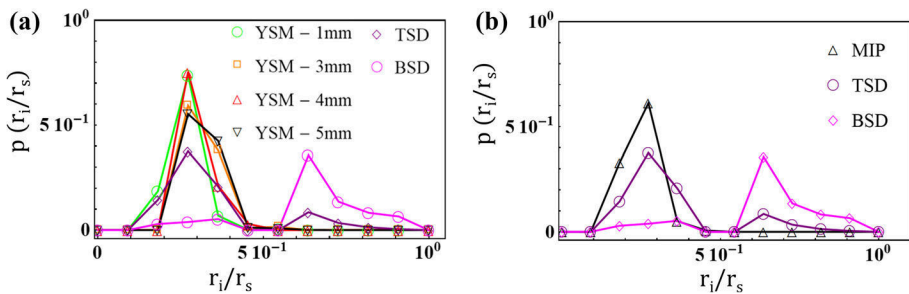
Fig. 8 Comparison between YSM, MIP and maximum inscribed ball method. **a** YSM versus maximum inscribed mall method, with TSD and BSD being the throat and body size distributions, respectively. **b** MIP versus maximum inscribed ball method

process in which mercury invades pores by the largest pore throats, while the directional character of flow experiments implies the influence of pore throats located both upstream and downstream of a given pore volume.

The capillary-bundle model used in the standard version of YSM is open to improvement in terms of topological and geometrical representativity. In this regard, the numerical simulations performed by Malvault et al. (2017) suggest that including the axial variation in the cross section of the capillaries can substantially improve the accuracy of the results provided by YSM, as it affects the pressure drop–flow rate relationship during injection of yield stress fluids. Nevertheless, such axial variation remains hardly accessible as an input to the method without resorting to auxiliary measurements. It should be noted that the capillary-bundle model is also used in most porosimetry techniques, such as MIP (Cieszko et al. 2019) or nitrogen porosimetry (Pomonis and Margellou 2018).

A new porosimetry method also based on the injection of non-Newtonian fluids through porous media was recently presented in the literature (Abou Najm and Atallah 2016; Atallah and Abou Najm 2019). This method was named ANA after the authors and provides the PSD of the equivalent bundle of capillary of a porous medium by using the results of M saturated infiltration experiments with water and $M-1$ with non-Newtonian fluids. Analogous to YSM, the total flow rate is interpreted as the combined signature of the contribution of all pore classes. The main difference lies in the inversion procedure, which consists in solving the system of 2 M equations expressing the total flow rate for each fluid as being equal to the sum of the contributions of the considered pore classes. This allows the computation of M pore classes r_i ($i=1...M$) and their corresponding M frequencies n_i. ANA method presents the advantage of not needing a yield stress, so the authors used Casson fluids in their experiments (Atallah and Abou Najm 2019). Nevertheless, ANA method also presents important drawbacks which complicate its experimental feasibility:

1. The solutions in terms of PSD provided by the method are not unique, given the fact that different combinations of pore sizes and frequencies result in the same flow rate under a given pressure gradient, as reported by Abou Najm and Atallah (2016).
2. Several fluids, including a Newtonian fluid, are needed in the tests. This adds complexity to the experimental set-up and requires not only a series of concentrations of the viscosifying agent giving thus different fluidity indices, but also previous accurate characterization of the shear rheology of each fluid. Moreover, this results in less available pore classes in the obtained PSD [typically four classes in the experiments presented by Atallah and Abou Najm (2019)]. It is noted that the use of a single fluid being injected at different values of pressure gradient may theoretically be possible. However, this alternative has not yet been experimentally validated.
3. The following condition needs to be imposed in ANA method in order to calculate the PSD:

$$\varepsilon V_T = \sum_{i=1}^{M} n_i \pi r_i^2$$

    with V_T being the total volume of the sample. This condition would be realistic only if the pore dimensions provided by the methods r_i were close to the dimensions of the pore bodies, which account for all the volume of the pores. However, both YSM and ANA provide pore dimensions that are close to the throat dimensions, so the preceding condition used in ANA is unrealistic in most porous media. YSM presents the advantage of not needing such condition in the algorithm used to calculate the PSD.

It is noted that YSM does not present the preceding limitations. However, despite the above-mentioned issues, the works of the latter authors confirm the great potential of non-Newtonian fluid flow to capture the signature of PSD in porous media.

Rodríguez de Castro (2019) recently presented a method to extend Darcy's law to the flow of spherical beads of equal size and the approach was experimentally validated. Despite the remarkable accuracy of the proposed Q versus ∇P predictions over more than 3 orders of magnitude (average error ~ 4% over the values of injection velocity ranging from 10^{-4} to 10^{-1} m/s), the errors were greater for the predictions performed at the low flow rates (average error ~ 25% over the values of injection velocity ranging from 10^{-5} to 10^{-4} m/s). This may be due to the fact that PSD is not used as an input to Darcy's law extension, while it is expected to have an influence at the lowest flow rates at which the fluid does not flow through all the pores. Consequently, higher accuracy levels at such low flow rates would require knowledge of the PSD, which is not readily accessible in some applications. Including the effects of PSD in Darcy's law would require further modelling efforts, e.g. through a permeability correction function taking into account the differences in terms of accessible pore volume for different values of the applied pressure gradient. In this regard, Chevalier and Talon (2015a, b) presented a numerical and experimental investigation addressing the critical behaviour of paths opening during flow of a yield stress fluid in porous media. Furthermore, Nash and Rees (2017) related the manner in which the breakthrough of a yield stress fluid begins to the PSD of the porous medium.

7 Conclusions

The present investigation was carried out in order to gather solid evidence on the effectiveness of YSM as a clean alternative to MIP. To do so, the particular case of model unconsolidated porous media with well-known geometry and controlled boundary conditions was specifically addressed. The approach consisted in comparing the results of a set of YSM laboratory tests to those obtained from numerical analysis of a digital image of a real pack of beads. In the procedure used to analyse the digital image, a modelled pore network was extracted and the body and throat size distributions were characterized. Then, a standard MIP test was numerically simulated by using the pore network as input geometry to obtain the PSD provided by this reference technique. This simulated test is an effective alternative to real MIP laboratory experiments with unconsolidated porous media, which require highly elaborate preparation of the samples.

The PSDs of four packs of equal spheres have been successfully characterized by applying the innovative YSM algorithm to raw flow rate–pressure drop laboratory measurements performed during injection of a yield stress fluid. The main finding is that the results provided by YSM are essentially identical to those obtained through numerical simulation of MIP. Furthermore, the agreement was also good when compared to numerical results previously reported in the literature. Therefore, the present results prove the reliability of YSM when applied to model unconsolidated media. Also, it has been shown, through comparison with the modelled pore network, that, as expected, the pore size distribution provided by YSM is closer to the distribution of the pore throats rather than the pore bodies. The observed small discrepancy may be attributed to the geometrical simplifications inherent to the network model of the complicated pore structure. Consequently, the present analysis has shed light on the understanding of the pore dimension being quantified by this method.

It is of particular interest to note that YSM supplies useful PSDs for these media despite being based on a simple bundle-of-capillaries model.

Although the results are promising, it must be borne in mind that the conclusions of this research only apply to packs of spherical beads of identical size, so the effects of statistical dispersion of the beads sizes and irregular grain shapes must still be evaluated. Numerical simulations combined with pore-network modelling should be considered as a powerful tool to achieve that goal. Also, a fundamental task consists in selecting a suitable injection fluid to experimentally characterize low-permeability media without significant alteration in the morphology of the porous medium (due to particle or polymer retention). Indeed, the present results prove that YSM can be considered as an alternative to MIP only in the range of higher sizes of pores when concentrated xanthan gum solutions are used as injected yield stress fluids. That being said, the current conclusions represent tangible progress in proving the experimental feasibility of YSM and an important step forward towards achieving substitution of MIP by a cleaner porosimetry technique.

References

Abou Najm, M.R., Atallah, N.M.: Non-Newtonian fluids in action: revisiting hydraulic conductivity and pore size distribution of porous media. Vadose Zone J. **15**(9), 1539–1663 (2016)

Agnaou, M., Lasseux, D., Ahmadi, A.: From steady to unsteady laminar flow in model porous structures: an investigation of the first Hopf bifurcation. Comput. Fluids **136**, 67–82 (2016)

Agnaou, M., Lasseux, D., Ahmadi, A.: Origin of the inertial deviation from Darcy's law: an investigation from a microscopic flow analysis on two-dimensional model structures. Phys. Rev. E **96**(4), 043105 (2017)

Alfi, M., Barrufet, M., Killough, J.: Effect of pore sizes on composition distribution and enhance recovery from liquid shale: molecular sieving in low permeability reservoirs. Fuel **235**, 1555–1564 (2019)

Ambari, A., Benhamou, M., Roux, S., Guyon, E.: Distribution des tailles des pores d'un milieu poreux déterminée par l'écoulement d`un fluide à seuil. C. R. Acad. Sci. Paris **311**(2), 1291–1295 (1990)

Atallah, N.M., Abou Najm, M.R.: Characterization of synthetic porous media using non-Newtonian fluids: experimental device. Eur. J. Soil Sci. **70**(2), 257–267 (2019)

Benmouffok-Benbelkacem, G., Caton, F., Baravian, C., Skali-Lami, S.: Non-linear viscoelasticity and temporal behavior of typical yield stress fluids. Carbopol, Xanthan and Ketchup. Rheol. Acta **49**, 305–314 (2010)

Bijeljic, B., Raeini, A., Mostaghimi, P., Blunt, M.J.: Predictions of non-Fickian solute transport in different classes of porous media using direct simulation on pore-scale images. Phys. Rev. E **87**(1), 013011 (2013)

Bultreys, T., De Boever, W., Cnudde, V.: Imaging and image-based fluid transport modeling at the pore scale in geological materials: a practical introduction to the current state-of-the-art. Earth Sci. Rev. **155**, 93–128 (2016)

Burlion, N., Bernard, D., Chen, D.: X-ray microtomography, application to microstructure analysis of a cementitious material during leaching process. Cem. Concr. Res. **36**, 346–357 (2006)

Carnali, J.O.: A dispersed anisotropic phase as the origin of the weak-gel properties of aqueous xanthan gum. J. Appl. Polym. Sci. **43**, 929–941 (1991)

Chauveteau, G.: Rodlike polymer solution flow through fine pores: influence of pore size on rheological behavior. J. Rheol. **26**, 111–142 (1982)

Chauveteau, G., Nabzar, L., El Attar, L., Jacquin, C.: Pore structure and hydrodynamics in sandstones. SCA Conference Paper Number 9607 (1996)

Chen, G., Lu, S., Zhang, J., Pervukhina, M., Liu, K., Wang, M., Han, T., Tian, S., Li, J., Zhang, Y., Xu, Ch.: A method for determining oil-bearing pore size distribution in shales: a case study from the Damintun Sag, China. J. Petrol. Sci. Eng. **166**, 673–678 (2018)

Chevalier, T., Talon, L.: Generalization of Darcy's law for Bingham fluids in porous media: from flow-field statistics to the flow-rate regimes. Phys. Rev. E **91**, 023011 (2015a)

Chevalier, T., Talon, L.: Moving line model and avalanche statistics of Bingham fluid flow in porous media. Eur. Phys. J. E **38**, 76 (2015b)

Chhabra, R.P., Richardson, J.F.: Non-Newtonian Flow and Applied Rheology: Engineering Applications. Butterworth-Heinemann/Elsevier, Amsterdam (2008)

Cieszko, M., Kempinski, M., Czerwinski, T.: Limit models of pore space structure of porous materials for determination of limit pore size distributions based on mercury intrusion data. Transp. Porous Media **127**(2), 433–458 (2019)

Dakhil, H., Auhl, D., Wierschem, A.: Infinite-shear viscosity plateau of salt-free aqueous xanthan solutions. J. Rheol. **63**(1), 63–69 (2019)

Dario, A.F., Hortencio, L.M.A., Sierakowski, M.R., Neto, J.C.Q., Petri, D.F.S.: The effect of calcium salts on the viscosity and adsorption behavior of xanthan. Carbohyd. Polym. **84**, 669–676 (2011)

Diamond, S.: Mercury porosimetry. An inappropriate method for the measurement of pore size distributions in cement-based materials. Cem. Concr. Res. **30**, 1517–1525 (2000)

Finney, J.L.: Random packings and the structure of simple liquids. I. The geometry of random close packing. Proc. R. Soc. Lond. A **319**, 479–493 (1970)

Finney, J.: Finney packing of spheres. Digital Rocks Portal, Digital Rocks Portal, 15 April 2016 (2016). http://www.digitalrocksportal.org/projects/47. Accessed 3 Dec 2018

Garcia-Ochoa, F., Santosa, V.E., Casas, J.A., Gómez, E.: Xanthan gum: production, recovery, and properties. Biotechnol. Adv. **18**, 549–579 (2000)

García-Ochoa, F., Casas, J.A.: Apparent yield stress in xanthan gum solutions at low concentrations. Chem. Eng. J. **53**, B41–B46 (1994)

Giesche, H.: Mercury porosimetry: a general (practical) overview. Part. Part. Syst. Charact. **23**, 1–11 (2006)

Gostick, J.: T: versatile and efficient pore network extraction method using marker-based watershed segmentation. Phys. Rev. E **96**(2), 023307 (2017a)

Gostick, J.T.: Versatile and efficient pore network extraction method using marker-based watershed segmentation. Phys. Rev. E **96**(2), 023307 (2017b)

Gostick, J., Aghighi, M., Hinebaugh, J., Tranter, T., Hoeh, M.A., Day, H., Spellacy, B., Sharqawy, M.H., Bazylak, A., Burns, A., Lehnert, W.: OpenPNM: a pore network modeling package. Comput. Sci. Eng. **18**(4), 60–74 (2016)

Gostick, J.T., Khan, Z.A., Tranter, T.G., Kok, M.D., Agnaou, M., Sadeghi, M., Jervis, R.: PoreSpy: a python toolkit for quantitative analysis of porous media images. J. Open Source Softw. **4**(37), 1296 (2019). https://doi.org/10.21105/joss.01296

Grattoni, C.A.: Influence of pore scale structure on electrical resistivity of reservoir rocks. PhD Thesis, University of London (Imperial College) (1994)

Hildebrand, T., Ruegsegger, D.: A new method of the model-independent assessment of thickness in the tree-dimensional images. J. Microsc. **185**(1), 67–75 (1997)

Houston, A.N., Otten, W., Falconer, R., Monga, O., Baveye, P.C., Hapca, S.M.: Quantification of the pore size distribution of soils: assessment of existing software using tomographic and synthetic 3D images. Geoderma **299**, 73–82 (2017)

Hudyma, N., Avar, B.B., Karakouzian, M.: Compressive strength and failure modes of Lithophysae-Rich Topopah spring tuff specimens and analog models containing cavities. Eng. Geol. **73**(1/2), 179–190 (2004)

Jones, D.M., Walters, K.: The behavior of polymer solutions in extension-dominated flows with applications to enhanced oil recovery. Rheol. Acta **28**, 482–498 (1989)

Khodja, M.: Les fluides de forage: étude des performances et considerations environnementales, PhD Thesis, Institut National Polytechnique de Toulouse (2008)

Kumar, A., Rao, K.M., Han, S.S.: Application of xanthan gum as polysaccharide in tissue engineering: a review. Carbohyd. Polym. **180**, 128–144 (2018)

León y León, C.A.: New perspectives in mercury porosimetry. Adv. Colloid Interface Sci. **76–77**, 341–372 (1998)

Li, X., Kang, Y., Haghighi, M.: Investigation of pore size distributions of coals with different structures by nuclear magnetic resonance (NMR) and mercury intrusion porosimetry (MIP). Measurements **116**, 122–128 (2018b)

Li, H., Li, H., Wang, K., Liu, Ch.: Effect of rock composition microstructure and pore characteristics on its rock mechanics properties. Int. J. Min. Sci. Technol. **28**(2), 303–308 (2018a)

Lindquist, W.B., Venkatarangan, A.: Pore and throat size distributions measured from synchrotron X-ray tomographic images of Fontainebleau sandstones. J. Geophys. Res. Solid Earth **105**(B9), 21509–21527 (2000)

Malvault, G., Ahmadi, A., Omari, A.: Numerical simulation of yield stress fluid flow in capillary bundles: influence of the form and the axial variation in the cross section. Transp. Porous Media **120**(2), 255–270 (2017)

Malvault, G.: Détermination expérimentale de la distribution de taille de pores d'un milieu poreux par l'injection d'un fluide à seuil ou par analyse fréquentielle, PhD thesis, Arts et Métiers ParisTech (2013)

Minagawa, H., Nishikawa, Y., Ikeda, I., Miyazaki, K., Takahara, N., Sakamoto, Y., Komai, T., Narita, H.: Characterization of sand sediment by pore size distribution and permeability using proton nuclear magnetic resonance measurement. J. Geophys. Res. **113**, B07210 (2008)

Mongruel, A., Cloitre, M.: Axisymmetric orifice flow for measuring the elongational viscosity of semi-rigid polymer solutions. J. Nonnewton. Fluid Mech. **110**, 27–43 (2003)

Nash, S., Rees, D.A.S.: The effect of microstructure on models for the flow of a bingham fluid in porous media: one-dimensional flows. Transp. Porous Media **116**(3), 1073–1092 (2017)

Nolan, G.T., Kavanagh, P.E.: The size distribution of interstices in random packings of spheres. Powder Technol. **78**, 231–238 (1994)

Oukhlef, A., Champmartin, S., Ambari, A.: Yield stress fluids method to determine the pore size distribution of a porous medium. J. Nonnewton. Fluid Mech. **204**, 87–93 (2014)

Oukhlef, A.: Détermination de la distribution de tailles de pores d'un milieu poreux, PhD thesis, Arts et Métiers ParisTech (2011)

Palaniraj, P., Jayaraman, V.: Production, recovery and applications of xanthan gum by *Xanthomonas campestris*. J. Food Eng. **106**, 1–12 (2011)

Pomonis, P., Margellou, A.: The pore length, the pore number and the pore anisotropy distributions in porous materials. Microporous Mesoporous Mater. **271**, 41–51 (2018)

Prodanovic, M., Lindquist, W.B., Seright, R.S.: Porous structure and fluid partitioning in polyethylene cores from 3D X-ray microtomographic imaging. J. Colloid Interface Sci. **298**, 282–297 (2006)

Rodríguez de Castro, A.: Flow experiments of yield stress fluids in porous media as a new porosimetry method. PhD thesis, Arts et Métiers ParisTech (2014)

Rodríguez de Castro, A.: Extending Darcy's law to the flow of Yield Stress fluids in packed beads: method and experiments. Adv. Water Resour. **126**, 55–64 (2019)

Rodríguez de Castro, A., Radilla, G.: Non-Darcian flow of shear-thinning fluids through packed beads: experiments and predictions using Forchheimer's law and Ergun's equation. Adv. Water Resour. **100**, 35–47 (2017a)

Rodríguez de Castro, A., Radilla, G.: Flow of yield and Carreau fluids through rough-walled rock fractures: prediction and experiments. Water Resour. Res. **53**(7), 6197–6217 (2017b)

Rodríguez de Castro, A., Omari, A., Ahmadi-Sénichault, A., Bruneau, D.: Toward a new method of porosimetry: principles and experiments. Transp. Porous Media **101**(3), 349–364 (2014)

Rodríguez de Castro, A., Ahmadi-Sénichault, A., Omari, A., Savin, S., Madariaga, L.-F.: Characterizing porous media with the yield stress fluids porosimetry method. Transp. Porous Media **114**(1), 213–233 (2016)

Rodríguez de Castro, A., Ahmadi-Sénichault, A., Omari, A.: Using xanthan gum solutions to characterize porous media with the yield stress fluid porosimetry method: robustness of the method and effects of polymer concentration. Transp. Porous Media **122**(2), 357–374 (2018)

Rouquerol, J., Baron, G., Denoyel, R., Giesche, H., Groen, J., Klobes, P., Levitz, P., Neimark, A.V., Rigby, S., Skudas, R., Sing, K., Thommes, M., Unger, K.: Liquid intrusion and alternative methods for the characterization of macroporous materials (IUPAC Technical Report). Pure Appl. Chem. **84**, 107–136 (2012)

Skelland, A.H.P.: Non-Newtonian Flow and Heat Transfer. Wiley, New York (1967)

Song, K.-W., Kim, Y.-S., Chang, G.S.: Rheology of concentrated xanthan gum solutions: steady shear flow behavior. Fibers and Polymers **7**, 129–138 (2006)

Sorbie, K.S.: Polymer-Improved Oil Recovery. Blackie and Son Ltd, Glasgow (1991)

United Nations: United Nations Environment Programme: Text of the Minamata Convention on Mercury for adoption by the Conference of Plenipotentiaries. The Conference of Plenipotentiaries on the "Minamata Convention on Mercury" (2013). http://www.mercuryconvention.org/. Accessed 12 Dec 2018

Wang, X., Hou, J., Song, S., Wang, D., Gong, L., Ma, K., Liu, Y., Liu, Y., Li, Y., Yan, L.: Combining pressure-controlled porosimetry and rate-controlled porosimetry to investigate the fractal characteristics of full-range pores in tight oil reservoirs. J. Petrol. Sci. Eng. **171**, 353–361 (2018)

Washburn, E.W.: The dynamics of capillary flow. Phys. Rev. **17**(3), 273 (1921)

Wildenschild, D., Sheppard, A.P.: X-ray imaging and analysis techniques for quantifying pore-scale structure and processes in subsurface porous medium systems. Adv. Water Resour. **51**, 217–246 (2013)

Withcomb, P.J., Macosko, C.W.: Rheology of xanthan gum. J. Rheol. **22**(5), 493–505 (1978)

Wu, H., Zhang, C., Ji, Y., Liu, R., Wu, H., Zhang, Y., Geng, Z., Zhang, Y., Yang, J.: An improved method of characterizing the pore structure in tight oil reservoirs: integrated NMR and constant-rate-controlled porosimetry data. J. Petrol. Sci. Eng. **166**, 778–796 (2018)

Yang, X., Mehmani, Y., Perkins, W.A., Pasquali, A., Schönherr, M., Kim, K., Perego, M., Parks, M.L., Trask, N., Balhoff, M.T., Richmond, M.C.: Intercomparison of 3D pore-scale flow and solute transport simulation methods. Adv. Water Resour. **95**, 176–189 (2016)

Zhang, N., He, M., Zhang, B., Qiao, F., Sheng, H., Hu, Q.: Pore structure characteristics and permeability of deep sedimentary rocks determined by mercury intrusion porosimetry. J. Earth Sci. **27**(4), 670–676 (2016)

Affiliations

Antonio Rodríguez de Castro[1] · Mehrez Agnaou[2] · Azita Ahmadi-Sénichault[3] · Abdelaziz Omari[4]

[1]   Arts et Métiers ParisTech, Rue Saint Dominique, 51006 Châlons-en-Champagne, France

[2]   Department of Chemical Engineering, University of Waterloo, 200 University Avenue, West Waterloo N2L 3G1, ON, Canada

[3]   I2M, Arts et Métiers Paris-Tech, CNRS, Esplanade des Arts et Métiers, 33405 Talence Cedex, France

[4]   I2M, Bordeaux-INP, CNRS, Esplanade des Arts et Métiers, 33405 Talence Cedex, France